Predicting hot electron generation in inertial confinement fusion with particle-in-cell simulations

S. H. Cao [1,2] D. Patel,[1,2] A. Lees,[1] C. Stoeckl,[2] M. J. Rosenberg,[2] V. Gopalaswamy,[1,2] H. Wen [2] H. Huang,[2]
A. Shvydky,[2] R. Betti,[1,2,3] and C. Ren[1,2,3,*]

[1]*Department of Mechanical Engineering, University of Rochester, Rochester, New York 14627, USA*
[2]*Laboratory for Laser Energetics, University of Rochester, Rochester, New York 14627, USA*
[3]*Department of Physics and Astronomy, University of Rochester, Rochester, New York 14627, USA*

A series of two-dimensional particle-in-cell simulations with speckled laser drivers was carried out to study hot electron generation in direct-drive inertial confinement fusion on OMEGA. Scaling laws were obtained for hot electron fraction and temperature as functions of laser/plasma conditions in the quarter-critical region. Using these scalings and conditions from hydro simulations, the temporal history of hot electron generation can be predicted. The scalings can be further improved to predict hard x-rays for a collection of OMEGA warm target implosions within experimental error bars. These scalings can be readily implemented into inertial confinement fusion design codes.

Success of inertial confinement fusion (ICF) requires a comprehensive understanding of laser plasma interactions (LPIs), which can affect the efficiency and uniformity of target implosion. A particularly important problem for direct drive is hot electron generation from LPIs. Hot electrons can preheat fuel to reduce the areal density and thwart ignition [1–4]. On the other hand, in the case of shock ignition [5,6] they can also deposit their energy in the compressed shell to enhance the ignition shock and assist ignition [7]. It is important to understand the physics and establish a predictive capability of hot electron generation. This capability is currently lacking.

There have been considerable efforts to measure hot electrons experimentally through the hard x-ray (HXR) signals they emit in the surrounding plasma, both at OMEGA [1,8–10] and at the National Ignition Facility (NIF) [11–13]. LPIs in the OMEGA experiments were shown to be dominated by two-plasmon decay (TPD) [14], where an electromagnetic wave decays into two electron plasma waves (EPWs) near $0.25n_c$, where n_c is the critical density [15–18]. Stoeckl *et al.* found that the measured HXR energy scaled exponentially with the overlapped intensity on OMEGA [9]. Froula *et al.* found the fraction of total hot electron energy to total laser energy $f_{\rm hot}$ scaled with $\eta \equiv (I_{14}\lambda_{\mu\rm m}L_{\mu\rm m}/T_{\rm keV})/81.86$, the TPD threshold parameter [18], where $T_{\rm keV}$ is the electron temperature T_e in keV, I_{14} is the laser intensity I in 10^{14} W/cm^2, $\lambda_{\mu\rm m}$ is the laser wavelength in microns, and $L_{\mu\rm m}$ is the density scale length L_n in microns, all at the $0.25n_c$ surface. Near the threshold $\eta \approx 1$, $f_{\rm hot}$ increased more rapidly with η and the increase became more gradual when η became large [19]. Hu *et al.* [20] similarly found that $f_{\rm hot}$ was a function of the common-wave convective gain, which is linearly proportional to η. However, from the basic physics point of view, it is an oversimplification to assume that $f_{\rm hot}$ depends on the

laser/plasma conditions only through the combination of η. Hot electrons originate from those electrons whose thermal velocities are close to the phase velocities of the plasma waves. The larger the background T_e, the more hot electrons can be generated. Therefore, $f_{\rm hot}$ cannot just depend on η, which decreases as T_e increases. Furthermore, in direct-drive implosions the laser/plasma conditions near $0.25n_c$ constantly evolve during the nanoseconds-long driving pulse, and TPD ($\eta > 1$) is present only in a fraction of the pulse. An implosion cannot be characterized by the peak η used in Refs. [19,20]. These experimental scalings are not sufficiently accurate to be used as a predictive tool.

In principle, the particle-in-cell (PIC) model [21] is fully nonlinear and kinetic and contains the essential LPI physics to predict hot electrons from first principles. In practice, the predictive capability of the PIC model is hampered by limited computational resources. Modeling that takes into account the interactions of multiple beams for the entire pulse duration, in full density range in three dimensions and with each beam consisting of a complex speckle pattern, is significantly beyond our current capabilities. Nevertheless, PIC simulations have been used to illustrate important physics such as staged acceleration [22], the three-dimensional (3D) nature of coexisting stimulated Raman side-scattering (SRSS) and TPD [23,24], and TPD saturation through Langmuir wave cavitation [25]. Using a reduced-description PIC code that precluded SRS, Vu *et al.* also found that $f_{\rm hot}$ depended on η as $1 - \exp\{[-(\eta - 1)^{0.5}]\}$ [25]. Fluid codes such as laser—plasma simulation environment (LPSE) [26] are computationally more efficient and have been used to study multibeam TPD with a common plasma wave [27]. LPSE also incorporates a test particle-based hot electron package, which was used to study laser smoothing effects and found $f_{\rm hot} \approx (\eta - 1.31)^{0.9}$ [28]. These kinetic or fluid simulations typically only modeled a window of a few tens of picoseconds near the peak η, not tracing the laser/plasma evolution over

---

*chuang.ren@rochester.edu

the entire nanoeconds-long driving pulses to systematically benchmark with experiments.

In this paper, we report an approach to predict hot electron properties that can be systematically benchmarked against experiments. We obtain hot electron scaling by fitting results from a series of two-dimensional (2D) PIC simulations with speckled laser drivers scanning different laser intensities, density scale lengths, and electron and ion temperatures near $0.25n_c$. Each simulation effectively models hot electron generation by TPD and backward SRS for a certain combination of laser/plasma conditions. Averaging over evolving laser/plasma conditions from hydrodynamic simulations, we can predict hot electron energy E_{hot} for an entire implosion from beginning to end. The predictions can be benchmarked directly with the data from HXR diagnostic. The benchmarking shows that an agreement within the experimental error bars can be achieved after a modification of the laser intensities from the hydro simulations. These results demonstrate the effectiveness of the approach to develop a hot electron prediction capability that can be incorporated into ICF design codes.

To obtain the hot electron scaling, a series of 2D PIC simulations using the code OSIRIS [29] were carried out within the parameter space corresponding to OMEGA warm target implosions where an extensive HXR database exists. These simulations employed a speckled laser pump propagating along the x direction with an intensity of I and a wavelength $\lambda_0 = 351$ nm and with its polarization in the simulation plane. Laser speckles were generated by the smoothing by spectral dispersion (SSD) [30] module in OSIRIS [31], which adopted the OMEGA parameters of a bandwidth of 360 GHz and f-number of 6.7. The number of speckles in the transverse direction was 20. CH plasma was used and the initial electron density (n_e) increased from $0.21n_c$ to $0.28n_c$ exponentially in the x direction. The density scale length L_n, defined to be $n_e/(\partial n_e/\partial x)$, was constant in the simulation box. The initial electron and ion temperatures T_e and T_i were uniform. The simulation box's length was proportional to L_n, with a dimension of $42.5(L_{\mu m}/150)\,\mu m \times 45.6\,\mu m$ [$3808 \times (L_{\mu m}/150) \times 4080$ cells]. The number of particles per cell was 200 (100 for the electrons and 50 each for the carbon and hydrogen ions). Boundary conditions in the longitudinal direction were open for the fields and thermal bath for the particles, and periodic in the transverse direction (y) for both the fields and particles. Collisions were enabled.

Each simulation can be viewed as a point in a parameter space whose coordinates are (L_n, I, T_e, T_i). An implosion is a line in this parameter space. A total of 108 simulations were performed with $100\,\mu m < L_n < 200\,\mu m$, 1.5×10^{14} W/cm$^2 < I < 3.0 \times 10^{14}$ W/cm^2, 1.5 keV $< T_e < 2.5$ keV and 0.8 keV $< T_i < 1.2$ keV. Among these, 86 simulations had $f_{hot} > 0.002$, where significant hot electrons, defined as electrons with kinetic energy over 50 keV, were observed. The scalings in this paper were obtained from these 86 runs.

SSD produces a beam full of speckles with different intensities and frequencies. These speckles have finite transverse widths and move at a time scale of picoseconds [32]. Figure 1(a) shows the laser speckles and the TPD plasma waves near $0.25n_c$ for a case with $\eta = 0.80$ (calculated using the average laser intensity). Although this η is well below the
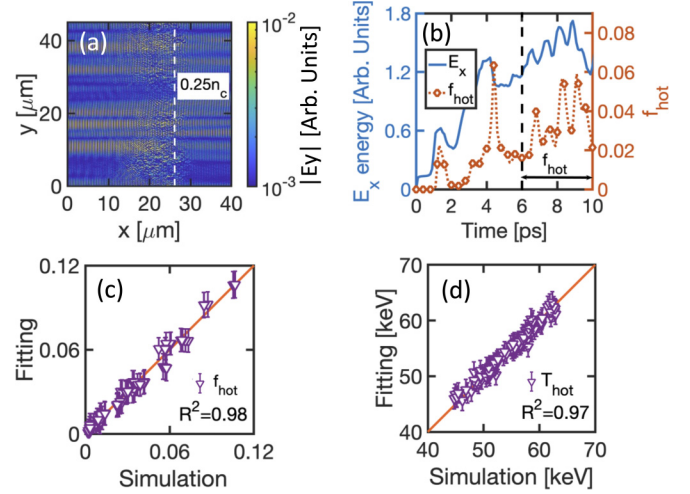

FIG. 1. (a) E_y component for both the laser speckles and TPD plasma waves at 8.0 ps. (b) Typical temporal evolution of hot electron fraction f_{hot} and plasma wave (E_x) energy. Plasma conditions for (a) and (b) are $L_n = 150\,\mu m$, $I = 2.5 \times 10^{14}$ W/cm^2, $T_e = 2.0$ keV, and $T_i = 1.0$ keV. (c) The fitting quality for the hot electron scaling f_{hot}, Eq. (1). (d) The fitting quality for the hot electron scaling T_{hot}, Eq. (2). Error bars in (c) and (d) show the 95% confidence interval for the fitting. We used *nlparci* from MATLAB to calculate the 95% confidence interval [33].

TPD threshold, TPD can still be excited by speckles with above-average intensities. Typical evolutions of the plasma wave energy and hot electron fluxes are plotted in Fig. 1(b), showing a steady state reached after $\sim$6 ps.

To systematically characterize the dependence of hot electron generation on the full set of parameters (L_n, I, T_e, T_i), we measured the hot electron energy fluxes as a fraction of the incident laser energy flux f_{hot}, using the time-averaged values after saturation to reduce the fluctuations from the small number ($\sim$60) of speckles used [Fig. 1(b)]. We then found a concise expression for f_{hot} through nonlinear regression, assuming that it is in the form of

$$\left\{ s_{0,0} + \sum_{x=1}^{2} s_{x,0} L_n^{s_{x,1}} T_e^{s_{x,2}} T_i^{s_{x,3}} I^{s_{x,4}} \right\}^{s_{0,1}},$$

where s are constants to be determined by regression against the simulation data. The nonlinear regression problem was solved in the least-square sense using the *lsqcurvefit* function in MATLAB [34]. We further rearranged the resultant expression using L_n, T_e, T_i/T_e, and the dimensionless TPD threshold parameter η [18]. Equation (1) shows the obtained scaling (units for L_n, T_e, and T_i are μm and keV),

$$\begin{aligned} f_{hot} \approx &\left\{ 6.7 - 3.1 \left(\frac{L_n}{150}\right)^{0.012} \left(\frac{T_e}{2}\right)^{0.17} \left(\frac{T_i}{T_e}\right)^{-0.0054} \eta^{-0.17} \right. \\ &\left. - 3.3 \left(\frac{L_n}{150}\right)^{0.034} \left(\frac{T_e}{2}\right)^{-0.30} \left(\frac{T_i}{T_e}\right)^{0.0053} \eta^{0.060} \right\}^{2.3}. \end{aligned} \quad (1)$$

The two exponential terms yielded a nonmonotonic dependence on the laser/plasma conditions. The fitting quality is plotted in Fig. 1(c) and the coefficient of determination was 0.98.

The hot electron temperature T_{hot} can also be obtained from the simulation data, with one exponential term,

$$T_{hot} \approx \left\{ 2.5 + 55 \left(\frac{L_n}{150} \right)^{0.092} \left(\frac{T_e}{2} \right)^{0.47} \left(\frac{T_i}{T_e} \right)^{0.033} \eta^{0.073} \right\} \text{keV}. \tag{2}$$

Its fitting quality is plotted in Fig. 1(d) and the coefficient of determination was 0.97.

To apply Eq. (1) to a realistic laser beam we need to account for various effects. Polarization smoothing (PS) [35] breaks laser speckles into two uncorrelated groups with mutually orthogonal polarizations. For each group we can choose the average intensity to be *half* of the average whole-beam intensity I_0, and the average hot electron fraction $\overline{f}_{hot}$ with PS is

$$\overline{f}_{hot} = f_{hot}(T_e, T_i, L_n, \eta_0/2). \tag{3}$$

Far-field intensity distributions of a single beam from distributed phase plates (DPPs) [36] on OMEGA are super-Gaussian, $I(r) = I_0 \exp[-(r/r_0)^n]$, where r is the radius, r_0 is the $1/e$ half width, and n is the super-Gaussian order. For a given phase plate, these parameters are fixed [37] and we can average $\overline{f}_{hot}$ over this intensity profile to include the effect of single-beam spatial intensity variation,

$$F_{hot} = \frac{\int_0^\infty \overline{f}_{hot} \cdot 2\pi r I dr}{\int_0^\infty 2\pi r I dr}. \tag{4}$$

The obtained F_{hot} was used for prediction.

OMEGA experiments use the HXR diagnostic to measure hot electron energy E_{hot} and temperature T_{hot} [38,39]. We used E_{hot} and T_{hot} to test the validity of the PIC scaling. Channel 2 of the OMEGA HXR detector, HXRD2, measures x-rays of energy in the 40–60 keV range with a time resolution of 100 ps and is suitable to test the predictive power of the PIC scaling in a time-resolved way.

For each OMEGA implosion, temporal laser/plasma conditions (I, L_n, T_e, T_i) were obtained from one-dimensional (1D) LILAC [40] simulations. The rate of E_{hot} increase is given as

$$dE_{hot}/dt = 4\pi R(t)^2 I_0(t) F_{hot}(t), \tag{5}$$

where R is the target radius at $0.25n_c$ from LILAC. Integrating over an entire pulse, we can predict E_{hot}.

Experimentally, the raw signal HXRD2, defined as the voltage measured by channel 2 of the OMEGA HXR detector, can be integrated to obtain the measured charge $Q = \int \text{HXRD2}/50\Omega \, dt$. Christopherson *et al.* found a simple fitting formula to relate the experimental E_{hot} in joules to Q in picocoulombs [28,41],

$$E_{hot} = Q/(-1.12 + 0.066T_{hot} + 0.00097T_{hot}^2), \tag{6}$$

where T_{hot} (in keV) is determined experimentally by fitting through HXR channels 2–4 [39]. We can also predict HXRD2 using HXRD2 $= 50\Omega \cdot (dQ/dt)$ and using Eq. (6) while holding T_{hot} constant,

$$\frac{dQ}{dt} = \left(-1.12 + 0.066T_{hot} + 0.00097T_{hot}^2 \right) \frac{dE_{hot}}{dt}, \tag{7}$$

where dE_{hot}/dt is from Eq. (5) with the required instantaneous T_{hot} from Eq. (2). Integrating Eq. (7), we can predict Q. Using Eq. (6) and the predicted E_{hot} and Q, we can predict an average T_{hot} for an entire shot.

We compared the predicted and experimental values of E_{hot}, HXRD2, Q, and T_{hot} for a collection of OMEGA shots of which good HXRD2 data and LILAC simulations were available. Predictions based on the original LILAC plasma conditions were represented by purple solid triangles in Figs. 2(a)–2(c), 2(e), and 2(f). Typical experimental uncertainties are 22% for E_{hot}, 10% for Q, and 9.4% for T_{hot} [39]. The predicted E_{hot} and Q largely tracked the data but with large mean relative errors of 47% and 43%, respectively. The predicted T_{hot} [Fig. 2(c)] did not track the data well. The predicted T_{hot} was in a narrow range because in these shots the plasma conditions, especially T_e, near the hot electron peak were in a narrower range than the range spanned by the simulations. The disagreement with the data reflects the limitations of these 2D simulations, which had a limited density range and speckle statistics and did not model stimulated Raman side scattering [23,24,42] that may generate hot electrons with a different T_{hot}. As shown below, we can use the experimental data to significantly improve these first principle-based predictions.

53% of the shots in Figs. 2(a)–2(c) were long pulses such as 96 010 in Fig. 2(d). Similar pulse shapes are used for cryogenic shots. We compared the predicted and measured time-resolved HXRD2 signal for 96 010 in Fig. 2(e), where the predicted signal overestimated at the peak. The HXRD2 peak seems to coincide with $\eta > 1$ (more on this later) and typical OMEGA peak η's are just above 1 [Fig. 2(e)]. This means the HXRD2 prediction can depend sensitively on the LILAC laser/plasma conditions, which cannot be experimentally measured. To further improve the predictions, we adopted an approach similar to Ref. [43] where LILAC predictions on neutron yield were improved through nonlinear regression using experimental data. We notice that previous work to include LPI in hydro simulations led to only slight or no changes in T_e and L_n [44]. For simplicity, we chose to study the effects of uncertainties in LILAC laser intensity at $0.25n_c I_0$. We aimed to map I_0 to a new I^* in the duration where TPD exists to narrow the gap between the predicted and measured data, by assuming

$$I^* = I_0 \left(w_{0,0} + \sum_{x=1}^{2} w_{x,0} L_n^{w_{x,1}} T_e^{w_{x,2}} T_i^{w_{x,3}} I^{w_{x,4}} R^{w_{x,5}} \right)$$
$$\times \{1.0 - \tanh[z_0 + (dR/dt)/z_1]\}/2.0.$$

The last tanh term was an activation function to determine the region where TPD can be observed. Coefficients (w, z) in this expression were determined by minimizing the mean relative error of Q.

We randomly picked 76% of the long pulse shots for training and 24% for validation. Using I^*, the mean relative error of E_{hot}, Q, and T_{hot} predictions all decreased to smaller than the experimental uncertainty [Figs. 2(a)–2(c) and Table I]. With the improved Q and E_{hot}, T_{hot} now tracks the data well [Fig. 2(c)]. The laser intensity modification was small [see η_0 and η^* in Fig. 2(e)] and the predicted HXRD2 signal became closer to the data. The modifications to the total laser
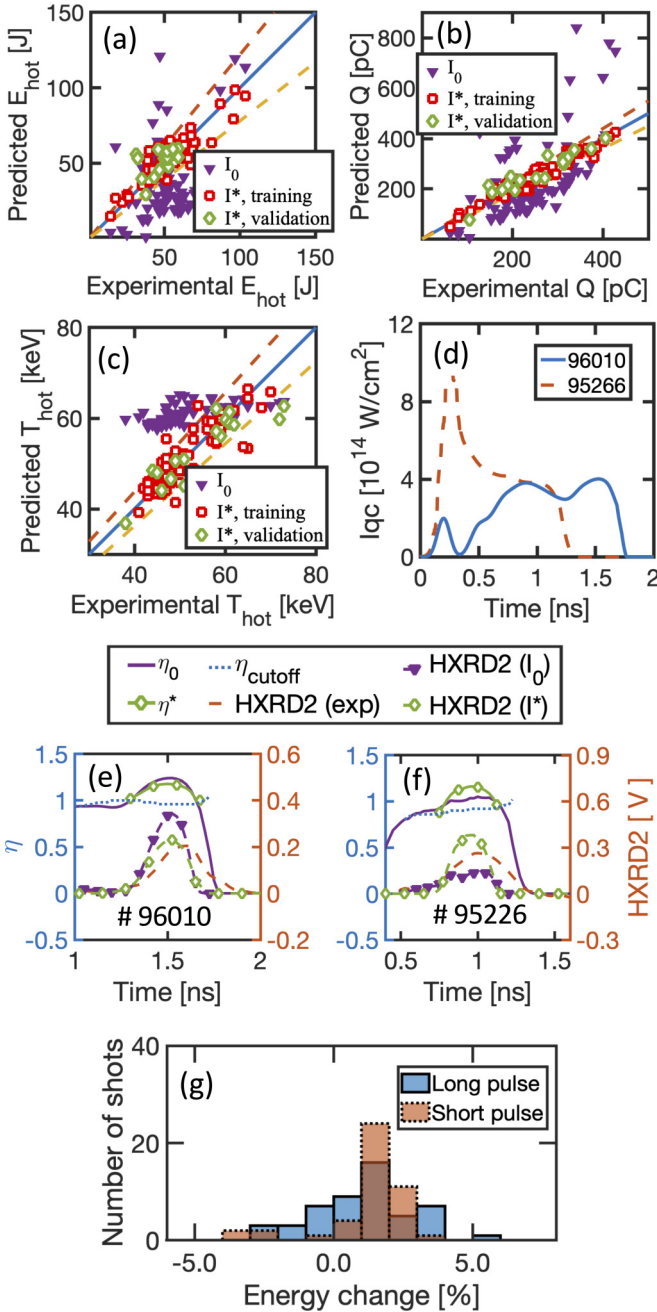
FIG. 2. (a) Predicted E_{hot} vs experimental data. (b) Predicted Q vs experimental data. (c) Predicted T_{hot} vs experimental data. Dashed lines in (a)–(c) represent the experimental error bars of 22% for E_{hot}, 10% for Q, and 9.4% for T_{hot}. In (a)–(c), "I_0" refers to the predictions based on the original laser-initiated liquid-assisted colloidal lithography (LILAC) laser intensity and "I^*" refers to the predictions based on the modified laser intensities, with "training" ("validation") referring to the group of shots that were (were not) used in deriving the laser intensity modification. (d) Laser intensity for shots 96 010 and 95 266. (e and f) Predicted and measured time-resolved HXRD2 signals and η from LILAC (η_0) and the modified intensity (η^*) for shots 96 010 (long pulse) and 95 226 (short pulse). We notice $I^*/I_0 = \eta^*/\eta_0$. (g) Histogram of laser energy change after modification.

TABLE I. Summary of the prediction errors and laser energy modification.

	E_{hot}	Q	T_{hot}	Laser energy change
Long pulse	9.7%	6.1%	5.3%	1.7%
Short pulse	13%	11%	4.4%	3.0%
Total	11%	8.3%	4.9%	2.3%

energy reaching $0.25n_c$ for all long pulse shots were small and centered around zero [Fig. 2(g)]. The average 1.7% change in the laser energy was small and within the LILAC uncertainty. The other shots in Figs. 2(a)–2(c) were short pulses, some with a high early intensity peak such as 95 226 in Fig. 2(d). They have very different characteristics compared with the long pulses, but their hot electrons can also be predicted with the same PIC scaling with an I^* trained by the data in the same way. The improved predictions also achieved an average error smaller than the experimental uncertainties [Fig. 2 and Table I]. The intensity modifications were larger than for the long pulses and were mostly increases [Fig. 2(g)], but the average laser energy change was still only 3%. We caution that the intensity modification was mainly a practical way to obtain a predictive capability. It may include a physical correction to the LILAC intensity. But it may also include corrections to the inaccuracies in E_{hot} and T_{hot} scalings from the imperfect 2D PIC simulations. Further studies, perhaps using a different data-assisted correction, are needed to disentangle the physics and improve the predictions.

The PIC scaling F_{hot} also gives a new interpretation to the long observation that HXR in OMEGA implosions strongly correlates with $\eta_0 > 1$ [14]. Here we used Eq. (4) to calculate η_{cutoff} that would generate above-noise-level HXRD2 signal and found $\eta_{cutoff} \approx 1$ for different shots [see Figs. 2(e) and 2(f)]. This shows that the threshold η for a speckled beam of a single polarization is effectively 0.5, not 1 [see Eq. (3)]. This η_{cutoff} depends on the particular speckle distribution and could be different from 1 with different SSD parameters. In addition, the results here show that hot electrons can be well predicted by treating the two laser polarizations as independent. This implies that the common-wave modes [27] would have limited effects on hot electron generation.

The hot electron scaling obtained here can be easily incorporated into hydro codes to better assess ICF target performance. It can also help the measurement of preheat in cryogenic shots [45]. Further improvement is possible using 3D simulations that can model the coexistence of stimulated Raman side scattering and TPD [23,24,46]. The hot electron scalings in this paper were based on the simulations and experimental data in the OMEGA parameter space. It is not clear whether they can be directly extrapolated to ignition scales. The much longer density scale length of ignition-scale plasmas poses the biggest obstacle to such extrapolation. Previous studies indicated that Raman side scattering may become more important in the NIF direct drive experiments [11,47]. The longer plasmas below $0.21 n_c$ may also cause more intensity modification to that from hydro simulations. This work

shows the general effectiveness of combining imperfect PIC simulations and data. We believe that the same approach can be applied to ignition-scale simulations and experiments to develop a hot electron prediction capability at ignition scale.

[1] V. A. Smalyuk, D. Shvarts, R. Betti, J. A. Delettrez, D. H. Edgell, V. Y. Glebov, V. N. Goncharov, R. L. McCrory, D. D. Meyerhofer, P. B. Radha *et al.*, Phys. Rev. Lett. **100**, 185005 (2008).

[2] V. N. Goncharov, T. C. Sangster, P. B. Radha, R. Betti, T. R. Boehly, T. J. B. Collins, R. S. Craxton, J. A. Delettrez, R. Epstein, V. Y. Glebov *et al.*, Phys. Plasmas **15**, 056310 (2008).

[3] R. S. Craxton, K. S. Anderson, T. R. Boehly, V. N. Goncharov, D. R. Harding, J. P. Knauer, R. L. McCrory, P. W. McKenty, D. D. Meyerhofer, J. F. Myatt *et al.*, Phys. Plasmas **22**, 110501 (2015).

[4] P. Radha, M. Hohenberger, D. Edgell, J. Marozas, F. Marshall, D. Michel, M. Rosenberg, W. Seka, A. Shvydky, T. Boehly *et al.*, Phys. Plasmas **23**, 056305 (2016).

[5] R. Betti, C. D. Zhou, K. S. Anderson, J. L. Perkins, W. Theobald, and A. A. Solodov, Phys. Rev. Lett. **98**, 155001 (2007).

[6] L. J. Perkins, R. Betti, K. N. LaFortune, and W. H. Williams, Phys. Rev. Lett. **103**, 045004 (2009).

[7] W. L. Shang, R. Betti, S. X. Hu, K. Woo, L. Hao, C. Ren, A. R. Christopherson, A. Bose, and W. Theobald, Phys. Rev. Lett. **119**, 195001 (2017).

[8] B. Yaakobi, C. Stoeckl, T. Boehly, D. Meyerhofer, and W. Seka, Phys. Plasmas **7**, 3714 (2000).

[9] C. Stoeckl, R. E. Bahr, B. Yaakobi, W. Seka, S. P. Regan, R. S. Craxton, J. A. Delettrez, R. W. Short, J. Myatt, A. V. Maximov *et al.*, Phys. Rev. Lett. **90**, 235002 (2003).

[10] B. Yaakobi, C. Stoeckl, W. Seka, J. Delettrez, T. Sangster, and D. Meyerhofer, Phys. Plasmas **12**, 062703 (2005).

[11] M. J. Rosenberg, A. A. Solodov, J. F. Myatt, W. Seka, P. Michel, M. Hohenberger, R. W. Short, R. Epstein, S. P. Regan, E. M. Campbell *et al.*, Phys. Rev. Lett. **120**, 055001 (2018).

[12] M. Rosenberg, A. Solodov, W. Seka, R. Follett, J. Myatt, A. Maximov, C. Ren, S. Cao, P. Michel, M. Hohenberger *et al.*, Phys. Plasmas **27**, 042705 (2020).

[13] A. Solodov, M. Rosenberg, W. Seka, J. Myatt, M. Hohenberger, R. Epstein, C. Stoeckl, R. Short, S. Regan, P. Michel *et al.*, Phys. Plasmas **27**, 052706 (2020).

[14] W. Seka, D. Edgell, J. Myatt, A. Maximov, R. Short, V. Goncharov, and H. Baldis, Phys. Plasmas **16**, 052701 (2009).

[15] M. N. Rosenbluth, Phys. Rev. Lett. **29**, 565 (1972).

[16] M. N. Rosenbluth, R. B. White, and C. S. Liu, Phys. Rev. Lett. **31**, 1190 (1973).

[17] C. S. Liu and M. N. Rosenbluth, Phys. Fluids **19**, 967 (1976).

[18] A. Simon, R. W. Short, E. A. Williams, and T. Dewandre, Phys. Fluids **26**, 3107 (1983).

[19] D. H. Froula, B. Yaakobi, S. X. Hu, P. Y. Chang, R. S. Craxton, D. H. Edgell, R. Follett, D. T. Michel, J. F. Myatt, W. Seka *et al.*, Phys. Rev. Lett. **108**, 165003 (2012).

[20] S. Hu, D. Michel, D. Edgell, D. Froula, R. Follett, V. Goncharov, J. Myatt, S. Skupsky, and B. Yaakobi, Phys. Plasmas **20**, 032704 (2013).

[21] C. K. Birdsall and A. B. Langdon, *Plasma Physics via Computer Simulation* (McGraw-Hill, New York, 1985).

[22] R. Yan, C. Ren, J. Li, A. V. Maximov, W. B. Mori, Z.-M. Sheng, and F. S. Tsung, Phys. Rev. Lett. **108**, 175002 (2012).

[23] H. Wen, A. V. Maximov, R. Yan, J. Li, C. Ren, and F. S. Tsung, Phys. Rev. E **100**, 041201(R) (2019).

[24] S. Cao, R. Yan, H. Wen, J. Li, and C. Ren, Phys. Rev. E **101**, 053205 (2020).

[25] H. Vu, D. DuBois, J. Myatt, and D. Russell, Phys. Plasmas **19**, 102703 (2012).

[26] J. F. Myatt, R. K. Follett, J. G. Shaw, D. H. Edgell, D. H. Froula, I. V. Igumenshchev, and V. N. Goncharov, Phys. Plasmas **24**, 056308 (2017).

[27] R. K. Follett, J. F. Myatt, J. G. Shaw, D. T. Michel, A. A. Solodov, D. H. Edgell, B. Yaakobi, and D. H. Froula, Phys. Plasmas **24**, 102134 (2017).

[28] D. Turnbull, A. Maximov, D. Cao, A. Christopherson, D. Edgell, R. Follett, V. Gopalaswamy, J. Knauer, J. Palastro, A. Shvydky *et al.*, Phys. Plasmas **27**, 102710 (2020).

[29] R. A. Fonseca, L. O. Silva, F. S. Tsung, V. K. Decyk, W. Lu, C. Ren, W. B. Mori, S. Deng, S. Lee, T. Katsouleas *et al.*, in *International Conference on Computational Science* (Springer, Berlin, Heidelberg, 2002), pp. 342–351.

[30] S. Skupsky, R. Short, T. Kessler, R. Craxton, S. Letzring, and J. Soures, J. Appl. Phys. **66**, 3456 (1989).

[31] H. Wen, F. S. Tsung, W. B. Mori, R. Fonseca, and L. Silva, Plasma Phys. Controlled Fusion **61**, 044007 (2019).

[32] J. Garnier and L. Videau, Phys. Plasmas **8**, 4914 (2001).

[33] MATLAB, nlparci, [EB/OL], https://www.mathworks.com/ help/stats/nlparci.html. Accessed September 12, 2021.

[34] MATLAB, lsqcurvefit, [EB/OL], https://www.mathworks.com/help/optim/ug/lsqcurvefit.html. Accessed September 12, 2021.

[35] T. Boehly, V. Smalyuk, D. Meyerhofer, J. Knauer, D. Bradley, R. Craxton, M. Guardalben, S. Skupsky, and T. Kessler, J. Appl. Phys. **85**, 3444 (1999).

[36] J. A. Marozas, J. Opt. Soc. Am. A **24**, 74 (2007).

[37] VISRAD, Distributed phase plates (DPPs) for Omega, [EB/OL], http://prism-cs.com/Manuals/VisRad/power_sources/phase_plate_params.html. Accessed February 7, 2022.

[38] C. Stoeckl, V. Y. Glebov, D. Meyerhofer, W. Seka, B. Yaakobi, R. Town, and J. Zuegel, Rev. Sci. Instrum. **72**, 1197 (2001).

[39] J. Trela, W. Theobald, K. Anderson, D. Batani, R. Betti, A. Casner, J. Delettrez, J. Frenje, V. Y. Glebov, X. Ribeyre *et al.*, Phys. Plasmas **25**, 052707 (2018).

[40] J. Delettrez, R. Epstein, M. Richardson, P. A. Jaanimagi, and B. L. Henke, Phys. Rev. A **36**, 3926 (1987).

[41] A. Christopherson, *Effects of Charged Particle Heating on the Hydrodynamics of Intertially Confined Plasmas* (University of Rochester Press, Rochester, 2020).

[42] C. S. Liu, M. N. Rosenbluth, and R. B. White, Phys. Fluids **17**, 1211 (1974).

[43] V. Gopalaswamy, R. Betti, J. P. Knauer, N. Luciani, D. Patel, K. M. Woo, A. Bose, I. V. Igumenshchev, E. M. Campbell, K. S. Anderson *et al.*, Nature (London) **565**, 581 (2019).

[44] J. Li, R. Yan, and C. Ren, Phys. Plasmas **24**, 052705 (2017).

[45] A. R. Christopherson, R. Betti, C. J. Forrest, J. Howard, W. Theobald, J. A. Delettrez, M. J. Rosenberg, A. A. Solodov, C. Stoeckl, D. Patel *et al.*, Phys. Rev. Lett. **127**, 055001 (2021).

[46] Y.-J. Gu, O. Klimo, V. Tikhonchuk, and S. Weber, Nucl. Fusion **61**, 066014 (2021).

[47] P. Michel, M. J. Rosenberg, W. Seka, A. A. Solodov, R. W. Short, T. Chapman, C. Goyon, N. Lemos, M. Hohenberger, J. D. Moody *et al.*, Phys. Rev. E **99**, 033203 (2019).